

# Effect of Substrate Bed Temperature on Solute Segregation and Mechanical Properties in Ti–6Al–4V Produced by Laser Powder Bed Fusion



S. PEDRAZZINI, M.E. PEK, A.K. ACKERMAN, Q. CHENG, H. ALI, H. GHADBEIGI, K. MUMTAZ, T. DESSOLIER, T.B. BRITTON, P. BAJAJ, E. JÄGLE, B. GAULT, A.J. LONDON, and E. GALINDO-NAVA

Titanium alloys are particularly sensitive to temperature during additive manufacturing processes, due to their dual phase microstructure and sensitivity to oxygen uptake. In this paper, laser powder bed fusion (LPBF) was used in conjunction with a heated substrate bed at 100 °C, 570 °C and 770 °C to produce specimens of Ti–6Al–4V, to investigate the change in mechanical properties and segregation of alloying elements. An initial increase in ductility was observed when increasing the temperature from 100 °C to 570 °C, followed by a significant loss in ductility when samples were produced at 770 °C. A suite of multi-scale characterisation techniques revealed that the as-printed microstructure was drastically different across the range of temperatures. At 100 °C,  $\alpha + \alpha'$  phases were identified. Deformation twinning was extensively observed in the  $\alpha$  phase, with Al and V segregating at the twin interfaces. At 570 °C (the most ductile sample),  $\alpha'$ ,  $\alpha$  and nano-particles of  $\beta$  were observed, with networks of entangled dislocations showing V segregation. At 770 °C, no martensitic  $\alpha'$  was identified. The microstructure was an  $\alpha + \beta$  microstructure and an increased volume fraction of tangled dislocations with localised V segregation. Thermodynamic modelling based on the Gibbs-free energy of formation showed that the increased V concentration at dislocations was insufficient to locally nucleate  $\beta$  phase. However,  $\beta$ -phase nucleation at grain boundaries (not dislocations) caused pinning of grain boundaries, impeding slip and leading to a reduction in ductility. It is likely that the increased O-content within specimens printed at increased temperatures also played a key role in high-temperature embrittlement. Building operations are therefore best performed below sub-transus temperatures, to encourage the growth of strengthening phases *via* solute segregation, and the build atmosphere must be tightly controlled to reduce oxygen uptake within the samples.

<https://doi.org/10.1007/s11661-023-07070-4>  
© The Author(s) 2023

S. PEDRAZZINI, M.E. PEK, A.K. ACKERMAN, Q. CHENG, T. DESSOLIER and T.B. BRITTON are with the Department of Materials, Imperial College London, South Kensington Campus, Exhibition Road, London, SW7 2AG, UK. Contact e-mail: a.ackerman14@imperial.ac.uk H. ALI is with the Department of Mechanical Engineering, University of Sheffield, Western Bank, Sheffield, S1 3JD, UK and also with the University of Engineering & Technology, Jamrud Road, Peshawar, Khyber Pakhtunkhwa, Pakistan. H. GHADBEIGI and K. MUMTAZ are with the Department of Mechanical Engineering, University of Sheffield. P. BAJAJ is with the Max-Planck Institute für Eisenforschung, Max-Planck Straße 1, 40237, Düsseldorf, Germany. E. JÄGLE is with the Max-Planck Institute für Eisenforschung and also with the Institute of Materials Science, Universität der Bundeswehr, Werner-Heisenberg-Weg 39, 85577 Neubiberg, Germany. B. GAULT is with the Department of Materials, Imperial College London and also with the Max-Planck Institute für Eisenforschung. A.J. LONDON is with the UK Atomic Energy Authority, Culham Science Centre, Abingdon OX14 3EB, UK. E. GALINDO-NAVA is with the Department of Materials Science and Metallurgy, University of Cambridge, 27 Charles Babbage Road, CB3 0FS, Cambridge, UK and also with the Department of Mechanical Engineering, Torrington Place, London, WC1E 7JE, UK. Manuscript submitted June 17, 2022; accepted April 25, 2023.

S. Pedrazzini and M. E. Pek have contributed equally.

## I. INTRODUCTION

LASER Powder Bed Fusion (LPBF) is an additive manufacturing (AM) process where a high-intensity laser melts and fuses selected regions of powders deposited in cross-sectional layers. The near net-shape production of components minimises the need for specialised tooling and allows the manufacture of increasingly complex designs, better tailored to the requirements of specific applications. These characteristics are very attractive for manufacturing high-performance alloys in the aerospace industry. Ti alloys, particularly Ti–6Al–4V (Ti-64), are used widely in the aerospace industry due to their high specific strength and hot corrosion resistance.<sup>[1]</sup> However, Ti alloys are expensive and time-consuming to produce using conventional cast and wrought methods.<sup>[2]</sup> LPBF is a viable alternative that allows the production of near-net shape bespoke components, reducing the cost and time of substantial machining.<sup>[3]</sup> However, several challenges

have prevented this technology from reaching optimal commercial implementation. For instance, Ti-6Al-4V produced by LPBF, without further treatments such as shot peening or hot isostatic pressing (HIP), showed reduced ductility and fatigue resistance compared with its counterpart produced by conventional methods.<sup>[4]</sup> This is due to surface roughness, porosity, and the fast cooling rates from 104 °C s<sup>-1</sup><sup>[3]</sup> up to 10<sup>6</sup> K s<sup>-1</sup><sup>[5]</sup> which generates high-residual stresses<sup>[6]</sup> and, more notably, the formation of highly textured, metastable martensitic structures in the as deposited condition.<sup>[7-9]</sup> These microstructures often include fine acicular  $\alpha'$  which forms within columnar  $\langle 100 \rangle$  prior  $\beta$  grains, which grow along the build direction.<sup>[10-12]</sup> This strong crystallographic texture affects the resulting mechanical strength of the material.

Common strategies to improve the mechanical properties of LPBF Ti-6Al-4V rely on post-production heat treatments designed to decompose the martensitic structure and relieve residual stresses.<sup>[7]</sup> Vilaro *et al.*<sup>[10]</sup> studied the microstructure produced by quenching from the  $\beta$  phase field and subsequent heat treatments at, above, and below the  $\beta$  transformation temperature (transus). The highest ductility values were obtained when tempering close to the martensite start temperature ( $M_s$ ), from 700 °C to 750 °C, and the resulting microstructure was a mixture of  $\alpha' + \beta + \alpha$  with lamellar morphologies. Other authors have found analogous microstructures and mechanical properties using similar heat treatments.<sup>[6-8,13,14]</sup> In addition, the use of multiple lasers in LPBF produced similar microstructures and mechanical properties.<sup>[15]</sup> Additional processes to reduce the residual stresses in LPBF-produced materials include methods such as shot peening<sup>[16]</sup> and hot isostatic pressing (HIP), which can also be used to reduce residual porosity.<sup>[17]</sup> These processes typically occur after an initial heat treatment.<sup>[18]</sup> In recent work, a heated base-plate was used *in-situ* during deposition, during LPBF production of Ti-6Al-4V to reduce residual stresses and decompose the martensitic structure.<sup>[19]</sup> Ali *et al.* found an increase in ductility with increasing temperature between 100 °C and 570 °C, then a subsequent decrease up to 770 °C.

Solute segregation in Ti alloys at interfaces and defects has not been widely studied. The subject of segregation at interfaces was discussed at length by Raabe *et al.*,<sup>[20]</sup> in which the authors discuss how segregation at interfaces and defects may be used beneficially to encourage the nucleation of additional phases. In Ti-64, Zen *et al.*<sup>[21]</sup> found that during recrystallisation, V content varies within primary alpha, but the hardness of the phase is governed by Al content. Semiatin *et al.* discuss how V is the controlling element in diffusion in Ti-64 and has a smooth concentration gradient away from the alpha-beta interface.<sup>[22]</sup> Ackerman *et al.*<sup>[23]</sup> have previously observed molybdenum segregation at grain boundaries in Ti-6Al-2Zr-4Sn-6Mo, and regularly spaced areas exhibiting elevated concentrations of Zr, thought to be segregating to localised defects.<sup>[24]</sup> In other alloy systems such segregation was also previously observed: in

nanocrystalline Al, it was suggested that oxygen pins the grain boundaries, limiting grain boundary movement.<sup>[25]</sup>

The present work employs advanced characterisation techniques, including SEM, TEM and APT, to characterise microstructural alterations resulting from elevated substrate temperatures including segregation at crystallographic defects. These solute concentration measurements at dislocations were then compared to a nucleation model: it is found that complex phase transition sequences and solute redistribution behaviour control the final microstructure, and these are not comparable to standard (room-temperature) LPBF-produced samples. These observations were used to elucidate the mechanisms controlling the strength, ductility and solute segregation behaviour at different substrate temperatures.

## II. EXPERIMENTAL METHODS

Gas-atomised powder of nominal chemical composition Ti-6Al-4V was provided by TLS Technik Spezialpulver and sieved to 15 to 45  $\mu\text{m}$  in diameter. The powders were used to manufacture 6 blocks, 30  $\times$  30  $\times$  10 mm in size, through LPBF on a pre-heated substrate at 100 °C, 370 °C, 470 °C, 570 °C, 670 °C and 770 °C. This was completed using a Renishaw SLM125 system with a modified pre-heating platform. The build was completed using the default Renishaw SLM parameters: laser focus offset 0, hatch spacing 0.08 mm, contour spacing 0.2, layer thickness 50  $\mu\text{m}$ , scanning strategy 90 deg alternative. The laser power and exposure time was varied between 120 and 200 W and 60 to 180  $\mu\text{s}$  respectively. Further details of production, residual stress measurements and porosity measurements have been published as part of a previous manuscript.<sup>[19]</sup> It has been assumed throughout the text that there is thermal stability within the build, so the bulk material is at the temperature of the heated bed, though there may be a slight thermal gradient within the material, hence specimens being extracted from similar locations for accurate comparison. Tensile specimens were separately printed and prepared in accordance with the ASTM standard E8/E8M-13a<sup>[26]</sup> with a gauge length of 50 mm on an Instron 5567B723, at a displacement controlled strain rate of 0.5 mm/min, equating to a strain rate of 10<sup>-4</sup> s<sup>-1</sup>, and were loaded with the tensile axis parallel to the build direction.

### A. Metallographic Preparation

Samples were sectioned for metallographic examination vertically along the  $x-z$  axis of the printed specimens (*i.e.*, perpendicular to the build direction) using a diamond saw, then hot-mounted in a mounting press at 190 °C for 8 minutes, in conductive bakelite (with carbon filler). They were polished initially with SiC grinding paper, then with 3 and 1  $\mu\text{m}$  diamond paste and finally 0.04  $\mu\text{m}$  colloidal silica to obtain a surface quality required for EBSD.

## B. Scanning Electron Microscopy (SEM) and Electron Backscatter Diffraction (EBSD)

Scanning electron microscopy (SEM) was performed on sections of the samples using a Zeiss Gemini SEM 300 microscope. A working distance of 8.5 mm was used, operating at a beam current of 3 nA and a voltage of 5 kV. A combination of secondary and backscattered electron imaging was used, to fully exploit the surface sensitivity and Z-contrast. Electron backscatter diffraction (EBSD) measurements were performed with a Bruker eFlash<sup>HD</sup> EBSD camera inside a FEI Quanta 650 scanning electron microscopy (SEM) using a beam acceleration voltage of 20 kV and a probe current of ~ 10 nA. Each sample was analysed with an EBSP resolution of 320 × 240 pixels, samples at 570 °C and 770 °C were analysed with a step size of 40 nm and an EBSD camera exposure of 25 ms while the sample at 100 °C was captured with a step size of 200 nm and an EBSD camera exposure of 70 ms. The differences in EBSD data collection was done to achieve a reasonable resolution with the respect to grain size.

## C. Transmission Electron Microscopy (TEM)

Transmission electron microscopy (TEM) was performed on 3 mm disc samples, which were cut using a diamond saw, then electropolished using a Struers Tenupol with a solution of 15 pct (by volume) perchloric acid in methanol, cooled with LN<sub>2</sub>. Each specimen was examined using a Technai Osiris microscope with a Bruker Energy-Dispersive X-ray detector (EDX). From the micrographs acquired, particle size distributions were determined through manual measurements. The matrix compositions of each specimen were measured by TEM-EDX, and any values presented here were obtained by taking the mean value over at least 10 measurements. Semi-quantitative data was obtained from EDX maps using the Cliff-Lorimer method.

## D. Atom Probe Tomography (APT)

Atom probe tomography (APT)<sup>[27]</sup> was performed on the samples using a LEAP 5000 XS in laser-pulsing mode. Specimens were prepared by *in-situ* lift out using a FEI Helios NanoLAB 600i dual-beam SEM-FIB, equipped with an Omniprobe micromanipulator. The Ga beam was used to prepare cantilevers, which were then welded onto the micromanipulator using Ga-beam deposited Pt, extracted and mounted onto Cameca Silicon flat-top coupons. Specimens were then sharpened using the Ga-beam until they were below 100 nm in diameter, then “cleaned” using a lower voltage of 5 kV Gallium, to minimise the ion beam damage caused by 30 kV implantation, by removing the affected region. Analysis conditions were varied based on the specimen’s profile within a selected range: temperatures between 40 and 60 K, laser energy in the range of 10 to 30 pJ, and a pulse frequency between 100 and 200 kHz. Reconstructions were performed using the Cameca Integrated Visualisation and Analysis Software (IVAS 3.8.4).<sup>[28]</sup>

## III. RESULTS

### A. Mechanical Characterisation

Tensile test results were published as part of a previous study<sup>[19]</sup> discussing the methods for alleviating internal stresses caused by additive layer manufacturing through heating the sample bed. Figure 1(a) summarises the values of ductility and how they are influenced by the substrate temperature. When the substrate was heated to 100 °C, the elongation was ~ 6 pct, which increased and peaked at ~ 10 pct at 570 °C, then sharply decreased to 0 pct (brittle failure, no ductility) at 770 °C. Figure 1(b) shows the change in ultimate tensile stress (UTS) with respect to substrate temperature. Figure 1(c) shows the full tensile curves of the material. Whilst samples printed at a bed temperature of 100 °C and 570 °C had similar curves, with minimal elongation at 100 °C, samples tested from a bed temperature of 770 °C were fully brittle.

### B. Microstructural Characterisation

EBSD was performed on the samples to better understand the mechanical testing observations, shown in Figure 2. After building a sample on a heated substrate at 100 °C, the microstructure consisted primarily of  $\alpha$  and  $\alpha'$  phases (as  $\alpha$  and  $\alpha'$  have similar lattice parameters and crystal structures, EBSD could not differentiate between them). Small pockets of  $\beta$  phase could be identified as shown by the EBSD phase map in Figure 2. EBSD also showed extensive presence of martensite, with the smallest grain size in the 100 °C sample. In comparison, the sample produced at 570 °C showed no alterations in grain size or  $\beta$  phase fraction. In the sample produced at 770 °C, the  $\alpha$  grain size increased.

### C. Compositional Analysis and Fine Scale Microstructure

Bright field TEM and EDX was performed on the samples and the results are shown in Figures 3 through 5. Figure 3 are micrographs and EDX maps of the sample produced at a substrate temperature of 100 °C. Microtwins were visible, though no diffraction was completed to assess whether, this has been inferred from the 60 deg angle between lathes, as described by Chen *et al.*<sup>[29]</sup> EDX maps could not resolve segregation of solutes at the microtwin boundaries.

The sample produced at a substrate temperature of 570 °C showed no microtwin boundaries (Figure 4) but EDX maps showed small quantities of nano-scale  $\beta$  phase (shown by the rejection of V from the  $\alpha$  phase in the EDX) which were too small to be identified by EBSD in Figure 2. There was a presence of dislocations which was not seen in the 100 °C specimen, which are more substantial within the  $\alpha$  lamellae.

The sample produced at a substrate temperature of 770 °C also had nano-scale faceted  $\beta$  grains, which can be assumed to be parent  $\beta$  left over from transformation (Figure 5). Figures 5(a) and (b) also showed networks of

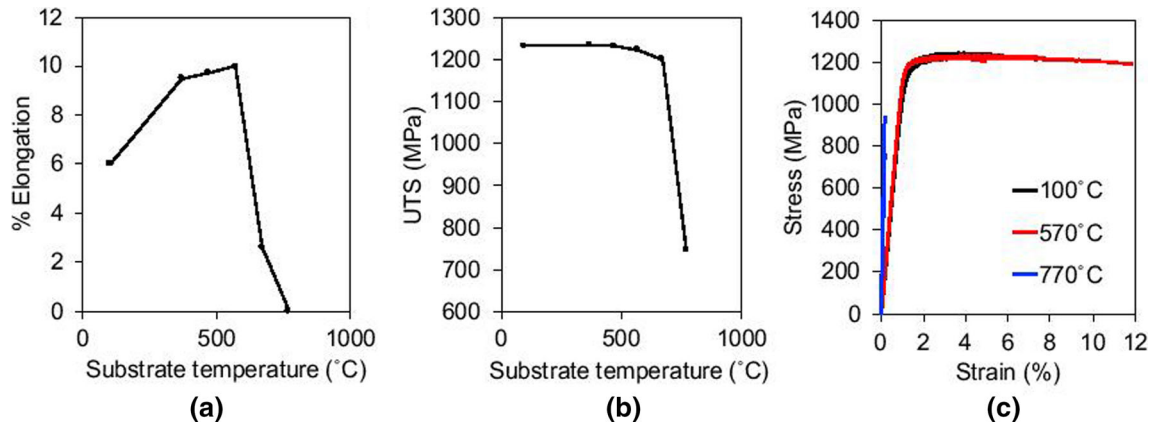


Fig. 1—(a) pct elongation vs substrate temperature during LPBF processing, measured during room temperature tensile tests, performed at  $10^{-4} \text{ s}^{-1}$  strain rate. (b) ultimate tensile strength (UTS) vs substrate temperature. (c) tensile curves for samples printed at a bed temperature of 100 °C (black), 570 °C (red) and 770 °C (blue) (Color figure online).

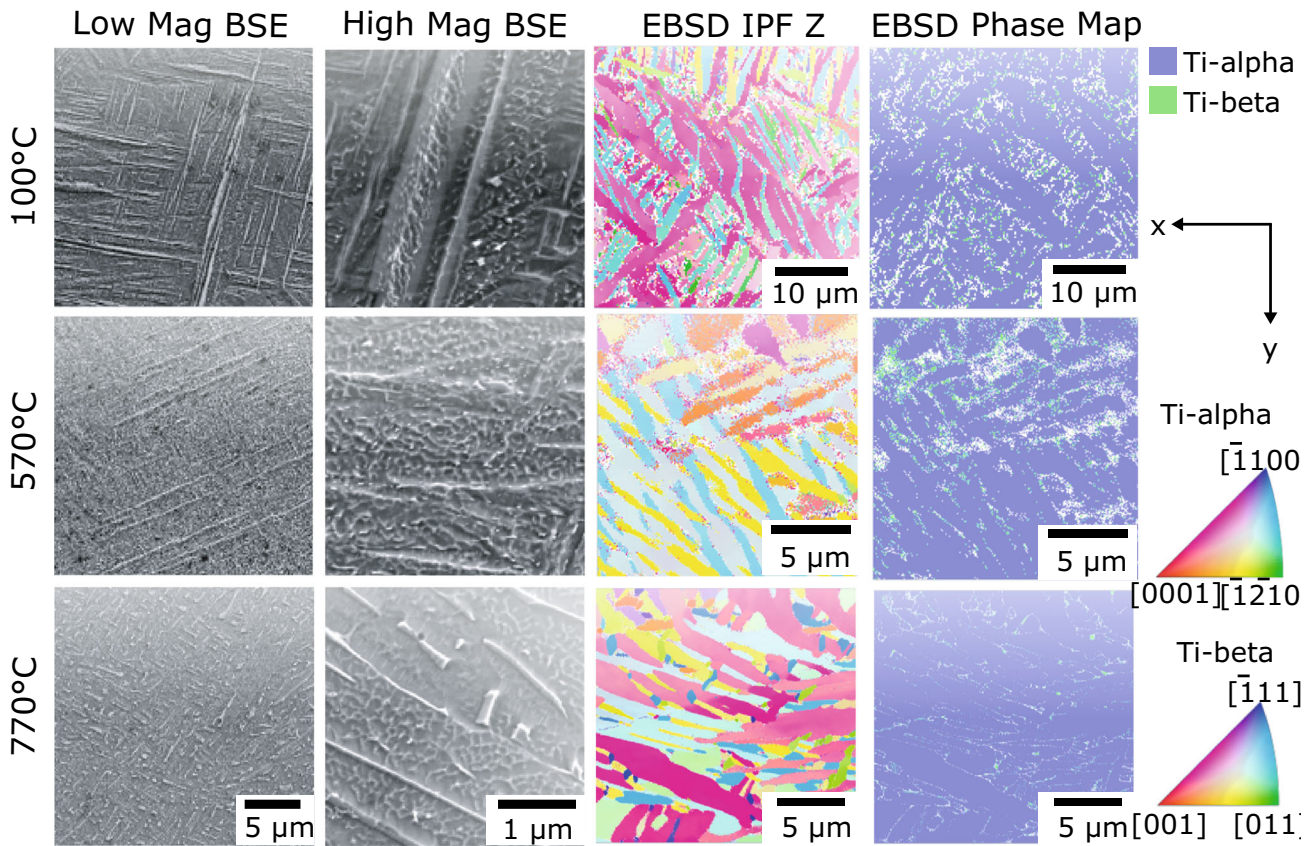


Fig. 2—Backscattered electron micrographs showing the overall microstructure of the LPBF printed samples and details of the phases present at higher magnification. Micrographs were taken from a central region of the  $x$ - $z$  axis (vertical sections). EBSD inverse pole figure (IPF) maps along the  $x$ -axis and a phase fraction map for each sample.

dislocations, tangled and evidently cross-slipped along specific crystal orientations, which were visible from the 60 deg angles between them (in this observed axis). Figures 5(c) and (g) through (h) show the nano-scale  $\beta$  phase. Figures 5(d) through (f) also showed that the dislocations have segregation of V and that V-rich phases, such as nano- $\beta$ , could be pinning dislocations. There was also evidence of Ti segregation along the

dislocation lines, Figure 5(d), which could again be affecting dislocation mobility.

#### D. Fine Scale Phase Segregation

To investigate the fine scale compositional variations, APT was used. Figure 6 shows an atom probe reconstruction from each sample. The local concentration of

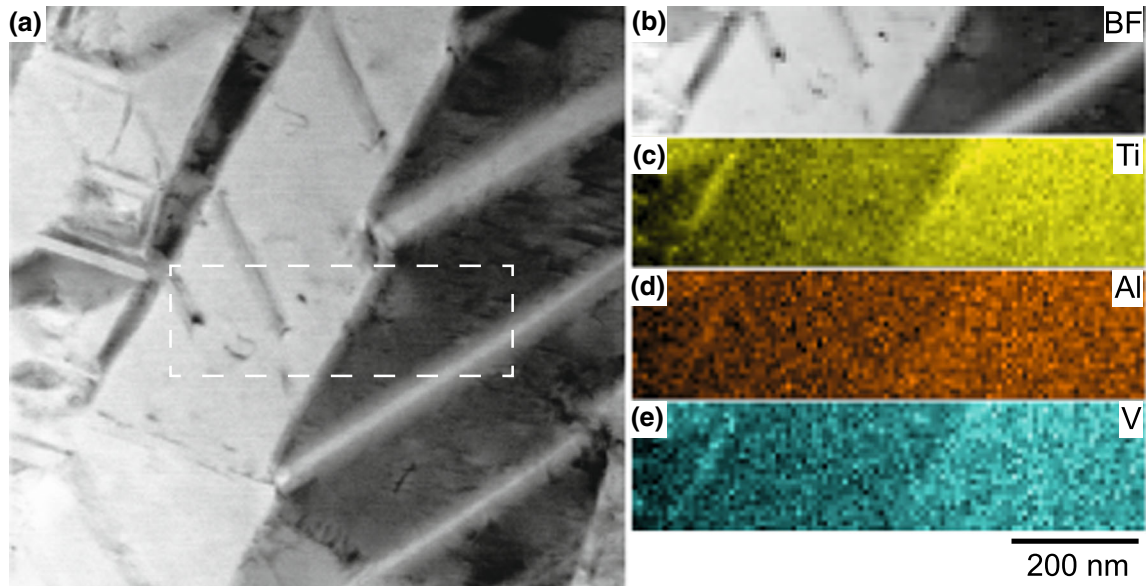


Fig. 3—STEM-EDX results of the sample produced at 100 °C. The foil was taken with the build axis out of the page. (a) STEM –BF with the dotted rectangle indicating the sampled EDX area; (b) Magnified STEM-BF; (c) Ti-K $\alpha$ ; (d) Al-K $\alpha$ ; (e) V-K $\alpha$ .

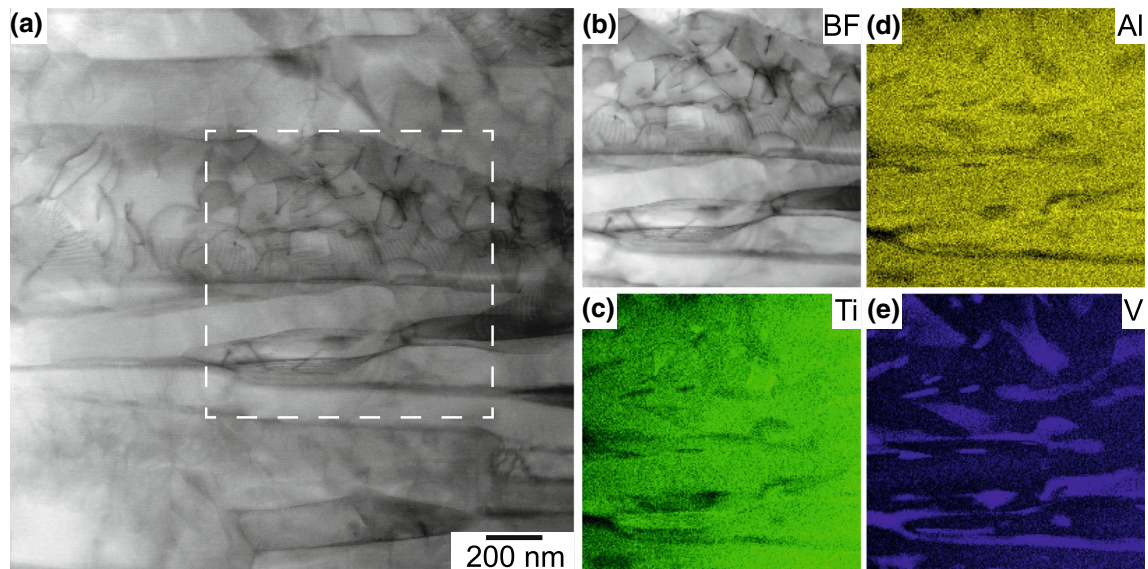
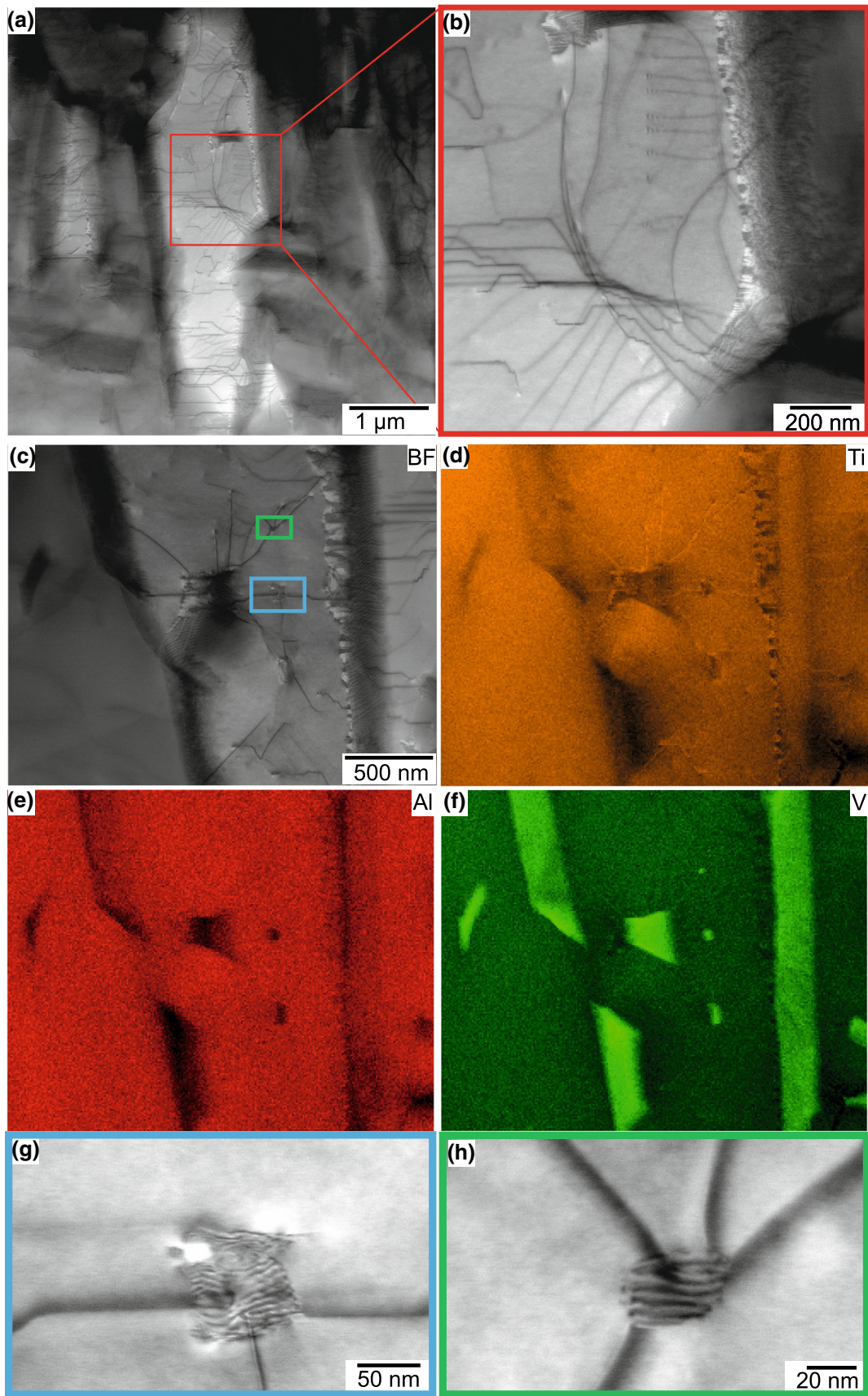


Fig. 4—STEM-EDX results of the sample produced at 570 °C. The foil was taken with the build axis out of the page. (a) STEM –BF with the dotted rectangle indicating the sampled EDX area; (b) Magnified STEM-BF; (c) Ti-K $\alpha$ ; (d) Al-K $\alpha$ ; (e) V-K $\alpha$ .

V and Al is shown as the iso-concentration surfaces of 4 and 12 at. pct, respectively, to allow a distinction between the  $\alpha'$ -Ti and  $\alpha$ -Ti phases, which have the same crystal structure but differ in chemical composition and lattice parameter.<sup>[30]</sup> The change in the relative amounts of  $\alpha'$ -Ti and  $\alpha$ -Ti across the three samples, especially between Figures 6(a) and (c), showed that the amount of  $\alpha'$ -Ti decreased with temperature, which was evident despite the small sampling volumes available in APT studies.

To obtain a quantitative breakdown of the elemental composition of each phase, a peak decomposition algorithm was applied to the mass spectra collected

through APT. The algorithm separated the contribution of each constituting element when two peaks overlapped, by using the relative natural abundances of isotopes of each element respectively. The composition values obtained for  $\alpha$ ,  $\alpha'$  and  $\beta$  measured on the sample produced at 570 °C, were compared with the literature for similar samples, albeit produced without the heated substrate. Furthermore, the other V and Al-rich regions labelled in Figure 6(b) as  $\alpha$  and  $\alpha'$ , matched the composition of  $\alpha$ -Ti and  $\alpha'$ -Ti found by Tan *et al.*<sup>[7]</sup> from observation of the 1D concentration profile. The composition of the three phases is tabulated in Table I, while the individual locations of phases were labelled in



◀Fig. 5—STEM-EDX results of the sample produced at 770 °C. (a) STEM -BF of 770 °C sample at low magnification to show  $\beta$  grain; (b) Magnified STEM-BF to show dislocation along preferential planes; (c) STEM -BF with (d) Ti-K $\alpha$ ; (e) Al-K $\alpha$ ; (f) V-K $\alpha$  (g to h) magnified view of two  $\beta$ -Ti grains highlighted in (c). The foil was taken with the build axis out of the page.

Figure 6. Table I also confirmed the absence of  $\beta$ -Ti in the sample produced at 100 °C, as the composition of V ( $\beta$  stabilising element) does not exceed 5 at. pct.

#### E. $\beta$ Phase Elemental Partitioning at 570 °C

A composition profile is calculated as a function of the distance to an iso-concentration surface delineating the  $\alpha$ -Ti phase. This is as proximity histogram and, as shown in Figure 7(b), it reveals solute partitioning of Ti and Al in  $\alpha$ -Ti and V in  $\beta$ -Ti. Oxygen preferentially partitioned to the  $\alpha$ -Ti phase while V was a  $\beta$ -Ti phase stabiliser. This matched Conrad's<sup>[31]</sup> findings that oxygen and nitrogen were  $\alpha$ -Ti stabilisers and preferentially partitioned to the  $\alpha$ -phase. A cylinder region of interest (ROI) was applied along a region of high V concentration just next to the  $\beta$ -Ti grain indicated with an arrow in Figure 7 to illustrate the solute segregation at an interface. This region of (relatively) high concentration was parallel to the grain boundary surrounding the large  $\beta$ -Ti grain, and could have been part of another, smaller  $\beta$ -Ti grain that was located at the very edge of the sample. 0.1 at. pct V and trace ( $<0.01$  at. pct) concentrations of Fe were detected along linear features, assumed to be dislocations, in the data set shown in Figure 7.<sup>[24,32]</sup> At the assumed dislocations, the measured ionic composition of  $O^+$  was estimated as  $0.016 < 0.020 < 0.024$  ionic pct (95 pct confidence interval). There was, however, a known peak overlap between  $TiO^+$  and  $O^+$  which could lead to an underestimation of the overall oxygen content. This peak overlap was analysed further using a custom Matlab program to enable localised (3D) isotopic deconvolution, therefore improving accuracy of the atom probe data measurements despite the known local overlap. This analysis showed  $\sim 80$  times more O from  $TiO^+$  than  $O^+$  and therefore that, in this case, the error margin introduced by the overlap was negligible.<sup>[33]</sup>

#### F. Segregation at Microtwins at 100 °C

Iso-density surfaces were applied to the reconstructions of the samples produced at a substrate temperature of 100 °C and 770 °C, to explore other microstructural features which were not evident in atom probe reconstructions in the absence of solute segregation, such as dislocations, grain boundaries or twin boundaries which the TEM micrographs suggested were segregated with Ti and V, as shown in Figures 3(c) and (e). The density iso-surfaces of Al and V in Figure 8(a) revealed planar surfaces that appeared only in specific crystallographic orientations, at  $\sim 60$  deg angles from each other, as expected of twin boundaries. These interfaces were measured by forming an iso-density surface and

observing the angle between them. There may be some error in this measurement due to differences in reconstruction parameters, such as concentration of the iso-surface formed and therefore the measured angle between them. The concentration profiles seen in Figures 8(b) and (c) are taken at 90° to the iso-surface to ensure we have sampled data through the feature with minimal angular effects. The angle between them suggested that the features followed specific crystallographic planes and, together with the micrographs in Figure 2(a), these could be assumed to be twin boundaries. The 1D concentration profiles in Figures 8(b) and (c) revealed that there were both Ti and Al segregation at each twin boundary.

#### G. Segregation at Dislocations at 770 °C

In the reconstruction of the sample produced at 770 °C, Ti and V iso-density surfaces delineating regions of high point density were added to reveal the segregation to linear features, which are assumed to be dislocations.<sup>[24,32]</sup> Both Ti and V could be pinning dislocations and therefore promoting lack of mobility, as observed in the TEM micrographs in Figures 5(c) through (f). A  $\beta$ -Ti particle was observed at the top right of the sample, with high-density columnar Ti regions oriented along the  $z$ -axis of the sample. The rod-like shape, coupled with the segregation matching the observations performed by TEM, suggested that these are dislocations, while the large quantity of high-density Ti region suggested a significant increase in dislocation density at 770 °C. The 1D composition profile in Figure 9(c) quantified through atom probe tomography the changes in composition previously detected by the STEM-EDX. It was noted that a similar feature to that of the V rich grain boundary was also found next to the  $\beta$ -Ti grain as per the 570 °C sample. The amount of oxygen in the reconstructions increased with printing powder bed temperature and could have affected the mechanical behaviour of the samples.

### IV. THERMODYNAMIC DRIVING FORCE FOR PHASE NUCLEATION FROM SOLUTE SEGREGATION AT DISLOCATIONS

To understand the presence of small pockets of  $\beta$  phase in various specimens (*e.g.*, Figure 5), solute segregation at dislocations was investigated. It was hypothesised that the increase in V at dislocations could increase the minimum energy needed for  $\beta$  nucleation, and therefore, encourage the nucleation and growth of the  $\beta$  phase below the typical transus, resulting in the formation of the small pockets of beta that were observed. In order for localised increases in phase stabilising elements to nucleate new phases, a critical dislocation density must be present to provide the driving force for nucleation. In this case, heterogeneous nucleation was considered.

The change in the Gibbs-free energy of nucleation,  $\Delta G$ , were described by Eq. [1]:

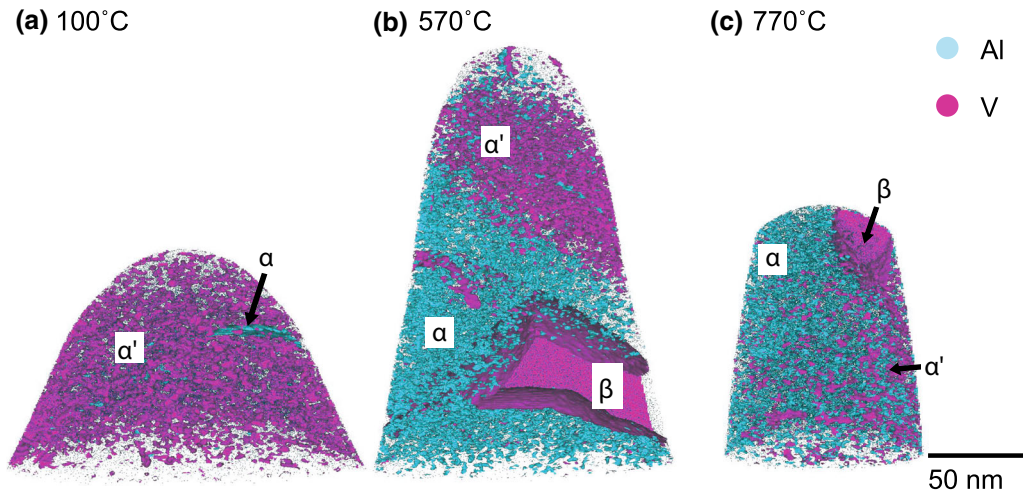


Fig. 6—APT reconstruction of the three samples. Isosurfaces of 4 at. pct V and 12 at. pct Al were applied. The 570 °C substrate sample (b) shows the clearest segregation of phases, while the 100 °C substrate sample (a) and 770 °C substrate sample (c) shows a majority of  $\alpha'$ -Ti and  $\alpha$ -Ti microstructure, respectively.

**Table I. Compositions (in at. pct) of  $\alpha'$ -Ti,  $\alpha$ -Ti and  $\beta$ -Ti Phases Obtained from APT Data, with Associated Standard Deviation Error**

Element	Alpha			Alpha Prime			Beta	
	100 °C*	570 °C	770 °C <sup>^</sup>	100 °C*	570 °C	770 °C <sup>^</sup>	570 °C	770 °C
Ti	bal.	bal.	bal.	bal.	bal.	bal.	bal.	bal.
Al	11.19 ± 0.95	10.46 ± 0.02	14.79 ± 0.34	6.92 ± 0.87	9.59 ± 0.01	10.94 ± 0.86	2.79 ± 0.00	3.07 ± 0.03
V	3.21 ± 0.31	2.37 ± 0.01	2.30 ± 0.19	3.85 ± 0.83	3.69 ± 0.01	5.13 ± 0.64	22.69 ± 0.01	22.43 ± 0.07
Cr	0.13 ± 0.08	0.28 ± 0.00	0.20 ± 0.08	0.14 ± 0.16	0.77 ± 0.00	0.91 ± 0.27	0.72 ± 0.00	0.15 ± 0.02
O	0.69 ± 0.23	0.76 ± 0.00	0.90 ± 0.02	0.67 ± 0.25	0.74 ± 0.00	1.26 ± 0.05	0.06 ± 0.00	0.20 ± 0.00
Fe	0.49 ± 0.23	0.00 ± 0.00	0.07 ± 0.03	0.40 ± 0.02	0.02 ± 0.00	0.04 ± 0.07	4.54 ± 0.01	2.60 ± 0.03

\*Denotes the use of a 1D concentration profile instead of decomposition of peaks. <sup>^</sup>Denotes the use of decomposition of peaks but with interfaces created by iso-concentration surfaces.

$$\Delta G = \frac{4}{3}\pi r^3 \Delta G_v S + 4\pi r^2 \gamma_{\alpha\beta} S + \frac{4}{3}\pi r^3 \Delta G_{el} S \quad [1]$$

where  $r$  is the radius of the nucleus,  $\Delta G_v$  is the volumetric driving force,  $\Delta G_{el}$  is the elastic strain energy,  $\gamma_{\alpha}$  is the interfacial energy between  $\alpha$  grains and  $\gamma_{\alpha\beta}$  is the interface energy between  $\alpha$  and  $\beta$  grains.

Nucleation of a new phase is only favourable if  $\Delta G$  is negative, as a system always wants to lower its total energy. To examine the nucleation model, interface energies and volumetric driving force were determined. The interface was assumed to be isotropic and incoherent. Gornakova and Prokofjev<sup>[34]</sup> proposed that interface energies of Ti-6Al-4V can be calculated by the Eqs. [2] through [4]:

$$\gamma_{\beta} = (449 \pm 10) - (0.385 \pm 0.096)(T - T_s) \quad [2]$$

$$\gamma_{\alpha} = (2200 \pm 164) - (1.48 \pm 0.20)T \quad [3]$$

$$\gamma_{\alpha\beta} = (1041 \pm 85) - (0.57 \pm 0.10)T \quad [4]$$

where  $T$  is the temperature in degrees Celsius and  $T_s$  is the solidus temperature, which is 1604 °C for Ti-64. The

interface energies at 570 °C (the heated bed temperature in experiments) were thus calculated to be 847.1 mJ/m<sup>2</sup> for  $\gamma_{\beta}$ , 1362.4 mJ/m<sup>2</sup> for  $\gamma_{\alpha}$  and 716.1 mJ/m<sup>2</sup> for  $\gamma_{\alpha\beta}$ .

The driving force for the nucleation of the  $\beta$  phase from the  $\alpha$  matrix is the difference in Gibbs free energy between the two phases. The Gibbs free energy of each phase of Ti-64 can be calculated by:

$$G^{\beta} = G^0 + G^{\text{ideal}} + G^{XS} \quad [5]$$

where

$$G^0 = X_{Al}G_{Al}^{\text{BCC}} + X_{Ti}G_{Ti}^{\text{BCC}} + X_VG_V^{\text{BCC}} \quad [6]$$

$$G^{\text{ideal}} = RT(X_{Al}\ln X_{Al} + X_{Ti}\ln X_{Ti} + X_V\ln X_V) \quad [7]$$

$$\begin{aligned} G^{XS} = & X_{Al}X_{Ti}(-125485 + 36.8394T) \\ & + X_{Al}X_V[(-95000 + 20T) + (-6000)(X_{Al} - X_V)] \\ & + X_{Ti}X_V[(10500 - 1.5T) + 2000(X_{Ti} - X_V) \\ & + 1000(X_{Ti} - X_V)^2] + X_{Al}X_{Ti}X_V[X_{Al}(116976.3 - 9.067T) \\ & + X_{Ti}(-175169 + 59T) + X_V(31107.3 - 42.316T) \end{aligned} \quad [8]$$



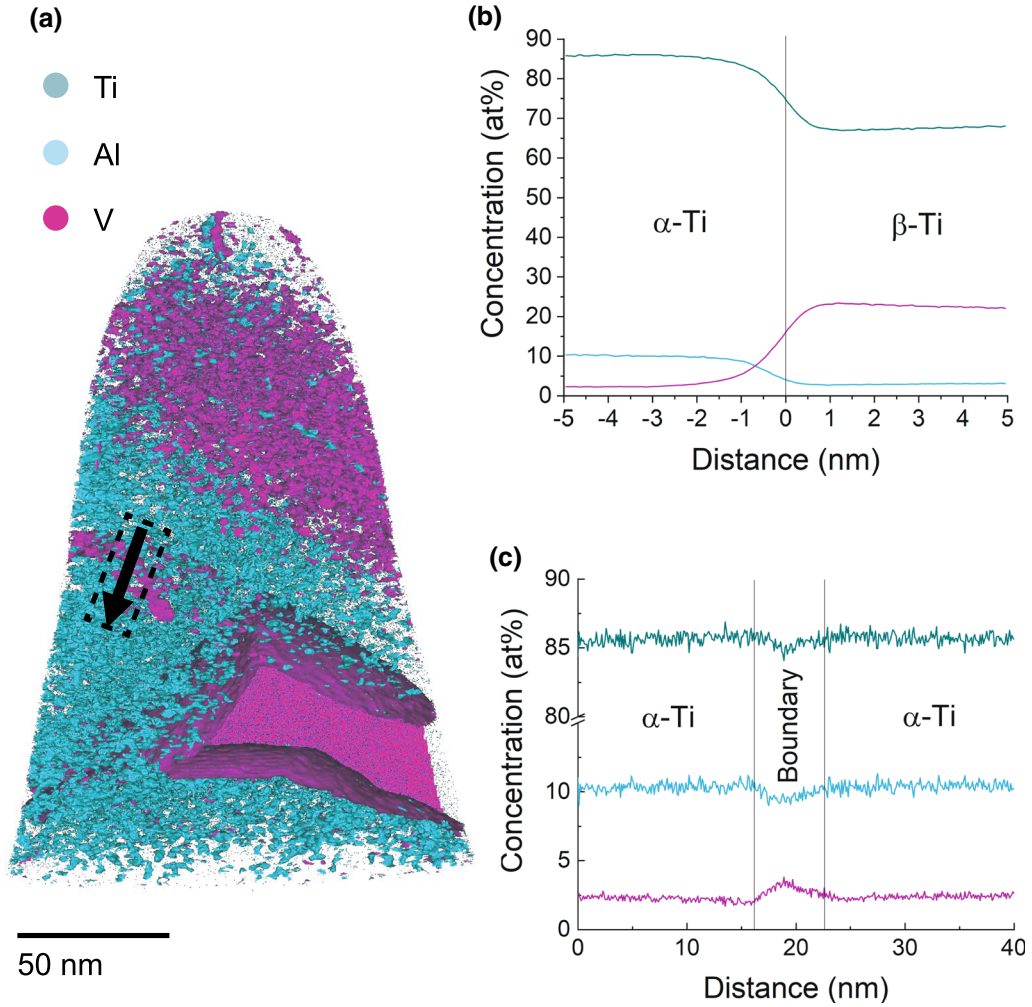


Fig. 7—APT reconstruction of the 570 °C substrate sample (a) with iso-concentration surfaces of 4 at. pct V and 12 at. pct Al applied, and the location of the cylinder region of interest (ROI) demarcated with an arrow. (b) proximity histogram about the large  $\beta$ -Ti grain on the bottom right of the sample, while (c) 1D concentration profile of the cylinder ROI indicated in (a).

Here,  $G^0$  is the Gibbs free energy of a mechanical mixture of the constituents,  $G^{\text{ideal}}$  is the entropy of mixing for an ideal solution,  $G^{XS}$  is the excess term and X is the mole fraction of each element in Ti-64.<sup>[35]</sup> The mole fraction of V, Ti and Al at the dislocation core was estimated to be 0.04, 0.86 and 0.1 respectively. Other parameters in the equations could be found from SGTE database.<sup>[36]</sup>

Figure 10, showed that below the  $\beta$  transus (980 °C/1253 K), the Gibbs free energy of the  $\alpha$  phase was always lower than that of  $\beta$  phase. Thus, the  $\alpha$  phase was always more stable and nucleation of  $\beta$  phase was unfavourable. However, Suprobo *et al.*<sup>[37]</sup> proposed that the presence of dislocations could raise the Gibbs free energy of  $\alpha$  phase and the contribution could be calculated by:

$$\Delta G_s = \varepsilon \rho V_m \quad [9]$$

where  $\varepsilon$  is the strain energy and  $V_m$  is the molar volume of Ti-64 ( $1.06 \times 10^{-5} \text{ m}^3/\text{mol}$ ). The strain energy was calculated by:

$$\varepsilon = \frac{\mu b^2}{4\pi} \ln \frac{R_e}{r} \quad [10]$$

where  $\mu$  is the shear modulus of Ti-64 ( $4.4 \times 10^{10} \text{ N/m}^2$ ),  $r$  is the radius of dislocation core which is assumed to be  $1 b$ , where  $b$  is the Burgers vector, and  $R_e$  is the outer cut-off radius of dislocation core ( $= \frac{1}{\sqrt{\pi\rho}}$ ).

To understand how the addition of dislocations in the matrix affects the Gibbs free energy, and the energy for nucleation of a new phase, the dislocation velocity and solute diffusion rate of V were calculated, as V was observed segregating to defects at 570 °C.

Dislocation velocity can be calculated by:

$$v = \frac{\varepsilon(\text{strain rate})}{\rho b} \quad [11]$$

where  $\rho$  is the dislocation density and  $b$  is the Burgers vector.<sup>[38]</sup> The strain rate,  $e$ , was assumed to be dependent of the cooling rate of  $30 \text{ }^\circ\text{Cmin}^{-1}$  and dependent the coefficient of linear expansion measured

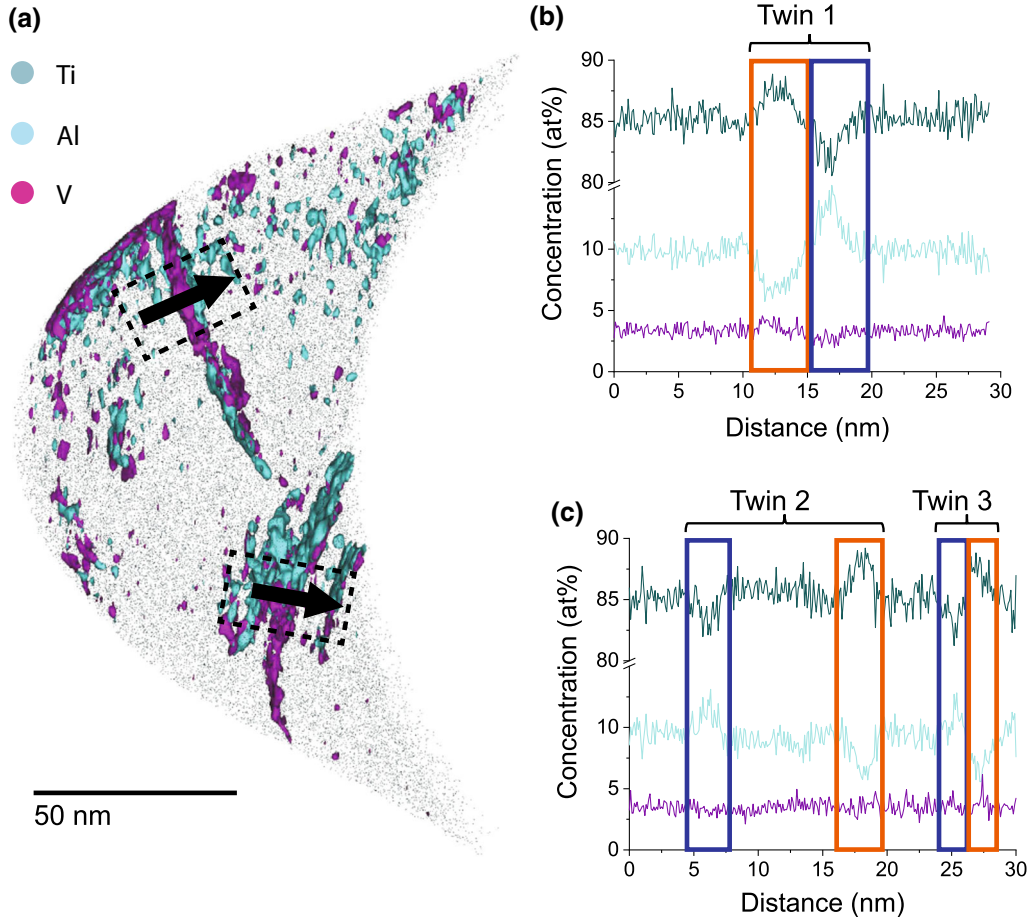


Fig. 8—(a) Density iso-surfaces of V  $2.65/\text{nm}^3$  (magenta) and Al  $6.90/\text{nm}^3$  (turquoise) were applied to the 100 °C substrate sample. Two cylindrical ROIs were added to investigate the planar surfaces, indicated by the dashed line boxes. (b) and (c) showed the 1D concentration profile of the two ROIs with their corresponding variation in elemental composition (Color figure online).

in SLM Ti-64 by Yang *et al.*<sup>[39]</sup> to be  $8.5 \times 10^{-6} \text{ C}^{-1}$ . The strain rate based on this was calculated to be  $4.35 \times 10^{-6} \text{ s}^{-1}$ . The dislocations were assumed to glide in the basal plane and the Burgers vector was found to be  $0.24 \times 10^{-9} \text{ m}$ . The dislocation density was estimated using the ‘line-intercept method’ to be  $1.09 \times 10^{14} \text{ m}^{-2}$ .<sup>[40]</sup> Thus, the dislocation velocity was calculated to be  $1.63 \times 10^{-10} \text{ m/s}$  at 570 °C.

The diffusion of V in  $\alpha$  matrix was assumed to be in a direction perpendicular to  $c$ -axis of the HCP lattice, as this was assumed to be the fastest path. The diffusion coefficient of steady state diffusion is normally represented by the Arrhenius equation:

$$D = D_0 \times e^{-\frac{Q}{RT}} \quad [12]$$

where  $D_0$  is the maximum diffusion coefficient at infinite temperature,  $Q$  is the activation energy,  $R$  is the gas constant and  $T$  is the temperature. For diffusion of V in  $\alpha$ -Ti at 570 °C,  $D_0$  was found to be  $2.33 \times 10^{-18} \text{ m}^2\text{s}^{-1}$  and  $Q$  was found to be 12,970.4 J.<sup>[41]</sup> However, Ti-64 is a ternary system, and Lindwall *et al.*<sup>[42]</sup> suggested that the presence of Al would affect the diffusion rate of V and the effect was shown by  $D_2 = 10^{-0.12\text{Al} + \log D}$ . The mole fraction of Al in Ti-64 was estimated to be 10 pct

and thus the experimental diffusion coefficient of V was calculated to be  $2.31 \times 10^{-20} \text{ m}^2/\text{s}$ . This, therefore, explains why V was observed decorating dislocations.

When the dislocation motion is controlled by the drag of solute atmosphere, which means that the solute cloud diffuses along with the dislocation and segregation occurs as shown by Figure 5, the relationship between the dislocation velocity and solute diffusion coefficient can be summarized by:

$$v = v_d \frac{\tau b^4}{kT} \exp\left(-\frac{U_d}{kT}\right) = D \frac{\tau b^2}{kT} \quad [13]$$

where  $\tau$  is the applied stress which is normally in the order of  $10^9 \text{ Pa}$ .<sup>[43]</sup> Applying a dislocation velocity of  $1.63 \times 10^{-10} \text{ m/s}$ , for solute segregation to occur the theoretical minimum diffusion coefficient of V was found to be  $3.33 \times 10^{-20} \text{ m}^2/\text{s}$ . The experimental diffusion coefficient ( $2.31 \times 10^{-20} \text{ m}^2/\text{s}$ ) is in agreement with the theoretical minimum.

By taking into account the contribution of dislocation strain, a new Gibbs-free energy curve for the  $\alpha$  phase was plotted as shown by the dashed blue curves in Figure 11.

At 570 °C, the Gibbs free energy of the  $\beta$  phase is greater than that of the  $\alpha$  phase by  $1.2253 \times 10^3 \text{ J/mol}$ .

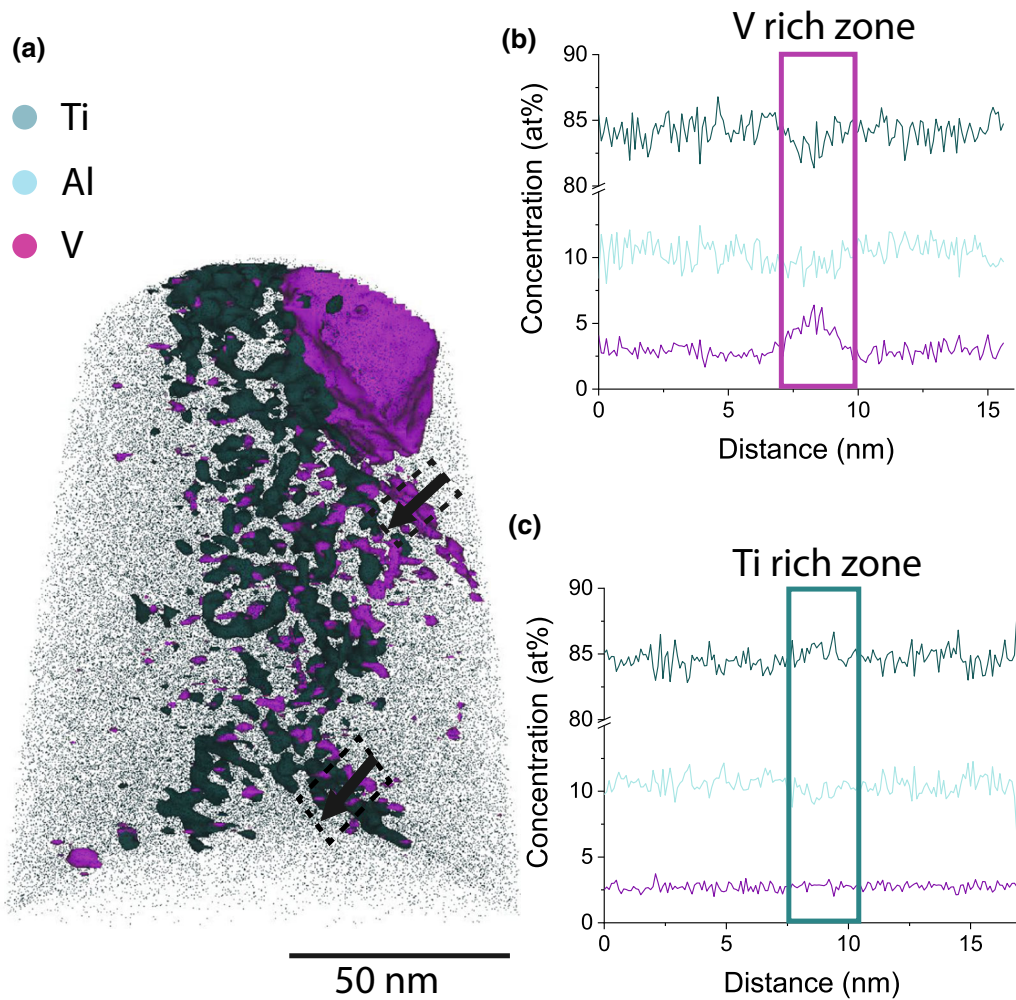


Fig. 9—(a) Density isosurfaces of V  $2.00/\text{nm}^3$  (magenta) and Ti  $51.50/\text{nm}^3$  were applied to the 770 °C sample. Two cylindrical ROIs were added to investigate a high-density V region next to the  $\beta$ -Ti grain on the top right and the high-density Ti region, indicated by the dashed line boxes, with their 1D concentration profiles plotted in (b) and (c), respectively (Color figure online).

In order to trigger nucleation of the  $\beta$  phase, the dislocation strain needs to raise the free energy of the  $\alpha$  phase by that amount. Using Eq. [9], the minimum dislocation density required was calculated to be  $4.6651 \times 10^{17}/\text{m}^2$ , Figure 11(a). The dislocation density found experimentally was  $1.09 \times 10^{14}/\text{m}^2$ , Figure 11(b), far smaller than the theoretical value. Thus, the Gibbs free energy of the  $\alpha$  phase does not meet the threshold energy for nucleation of the  $\beta$  phase at the observed dislocation density. The printer bed temperature has been used for the temperature of the bulk material, though a thermal gradient may be present, which could account for error within the calculations.

## V. DISCUSSION

### A. Effect of Substrate Temperature on Microstructure Evolution

One of the most noteworthy results from this work were the significant differences in the microstructure when varying the substrate temperatures. Table II

summarises such changes. As described previously,  $\alpha$  was differentiated from  $\alpha'$  due to the compositional changes in the different phases. At 100 °C, less  $\beta$  formed and there was a proportionately higher phase fraction of  $\alpha'$ . The microstructure contained both  $\alpha$  and  $\alpha'$ , and had a lower dislocation density than the other two conditions. The rapid cooling rate after solidification provided the necessary driving force for large scale  $\beta$  to  $\alpha$  and  $\alpha'$  transformation<sup>[31]</sup> and showed a fast cooling microstructure with the presence of microtwins.<sup>[44]</sup> Microtwinning here is likely due to the residual stress resulting from the phase transformation, and can be a result of intrinsic stacking faults.<sup>[45]</sup> The very low fraction of  $\beta$  phase was likely due to rapid transformation kinetics and reduced diffusion at 100 °C, resulting in a large amount of  $\beta$  to  $\alpha$  transformation. In addition, microtwins with both Al and V rich regions were identified, though Al and V did not co-segregate at the interface. This indicated that short range diffusion was occurring due to the formation of microtwins within the alloy, leading to a partitioning effect towards forming  $\alpha$  and  $\beta$  in the Al- and V-rich regions; a mechanism which

was seen experimentally in other alloy systems.<sup>[35,36,46]</sup> Microtwins were a result of the high lattice strains and low symmetry between the  $\alpha$  and  $\beta$  phases,<sup>[47]</sup> therefore chemical segregation occurred, as observed in our work.

Upon increasing the substrate temperature to 570 °C, no evidence of microtwinning was found. Instead, nano-scale  $\beta$  phases, which are likely to be remnant parent  $\beta$  phase were observed within  $\alpha'$  and  $\alpha$ . The ductility was the highest of all 3 samples discussed here. Dislocation networks were observed within the  $\alpha$  lamellae, likely due to the absence of microtwinning and the presence of  $\beta$  phase at the  $\alpha$ -grain boundaries. Interfacial dislocations in Ti-64 have been known to form at the (moving)  $\alpha'/\beta$  interface as  $\alpha'$  nucleates and grows

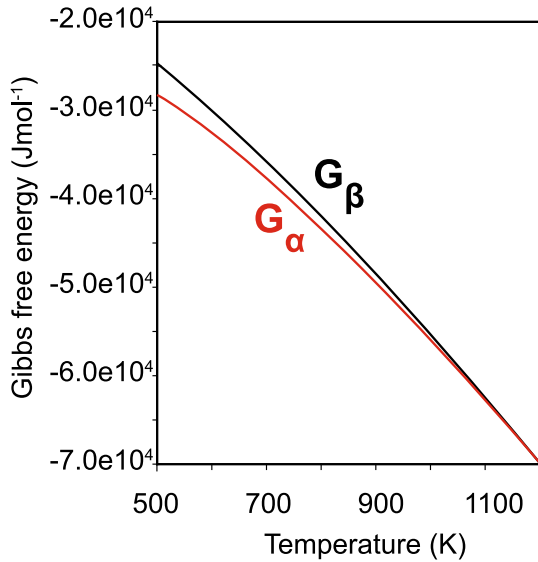


Fig. 10—Variation of Gibbs-free energy with temperature, where  $G_\alpha$  represents the Gibbs free energy of the  $\alpha$  phase and  $G_\beta$  represents the Gibbs-free energy of the  $\beta$  phase.

(during the solid-state transformation), due to the high shear strain of the martensitic transformation and the high local lattice mismatch between  $\alpha'$ ,  $\alpha$  and  $\beta$  phases. The substrate temperature was sufficient to promote dislocation recovery, however, the remnant  $\beta$  at the grain-boundary inhibited significant dislocation annihilation leading to local dislocation reconfiguration taking place instead. The networks of dislocations formed could act as “soft barriers” for slip, therefore influencing mechanical properties.<sup>[48]</sup> Using the analogy of dislocation networks forming in single-crystal (SX) Ni-based superalloys, Rai *et al.* have observed that the formation of dislocation networks at the  $g/g'$  interfaces promotes strain localisation and material softening under low-cycle fatigue<sup>[49]</sup>; the deformation temperature was 850 °C, preventing directional coarsening, and therefore dislocation reconfiguration was primarily driven by the interfacial misfit and deformation within the matrix. In the present case, the dislocation networks promoted an increase in ductility by allowing more plasticity to take place locally within the  $\alpha$  lamellae, whereas the fine grain boundaries and nano- $\beta$  compensated for the local softening and kept the macroscopic strength high. Textures that have a high likelihood of  $\langle a \rangle$  type dislocations, which could transfer easily between  $\alpha$  lamellae, are more ductile, though the EBSD in Figure 2 is insufficient to make this assumption. Similar Ti microstructures exhibit this behaviour, which may explain some of the tensile results observed here.<sup>[50,51]</sup>

At 770 °C, there were significant changes in mechanical properties, also reflected in the dislocation content and phase structure. A rapid drop in ductility was observed. There was a higher phase fraction of  $\beta$  within this sample and less  $\alpha'$  remained. However, these changes alone do not account for a complete loss in ductility. Dislocation tangles were observed in Figure 8: these could be formed by a similar mechanism as the dislocation networks at 570 °C, but the higher build temperatures could promote extensive recovery and

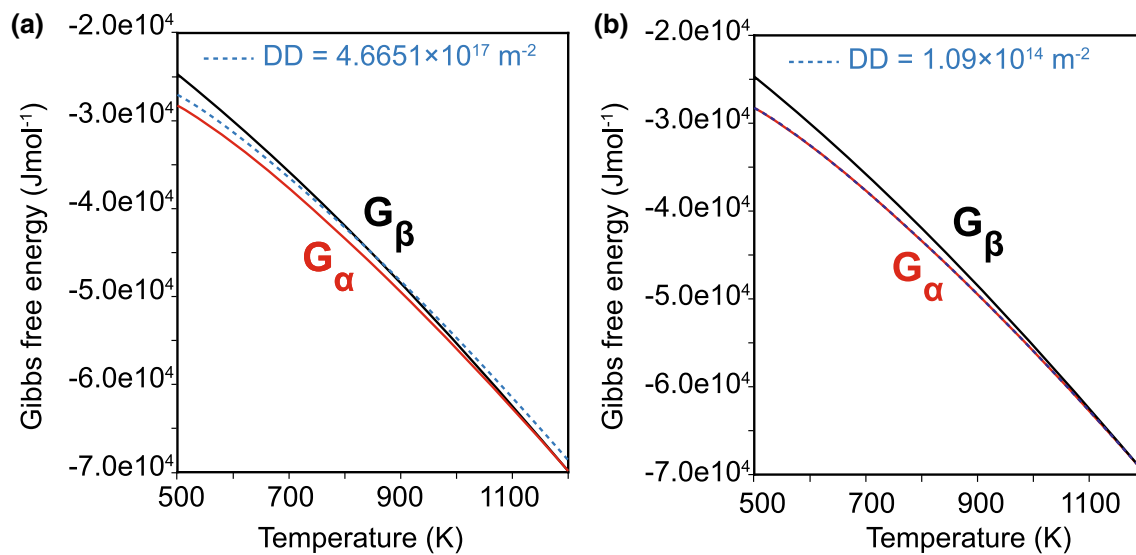


Fig. 11—Variation of Gibbs-free energy with temperature when dislocation density is (a)  $4.6651 \times 10^{17}/\text{m}^2$  and (b)  $1.09 \times 10^{14}/\text{m}^2$ .

**Table II. Summary of Observed Results Dependent on Substrate Temperature**

	100 °C	570 °C	770 °C
Primary Phases	$\alpha' + \alpha$	$\alpha' + \alpha + (\text{nano})\beta$	$\alpha + \beta$
Crystal Defects	twinning	dislocation networks	dislocation tangles
Solute Behaviour	Al, V segregation at twins	V segregation at dislocations	V segregation at dislocations

partial loss of the networks. The high density of dislocation networks observed in the vicinity of the  $\alpha/\beta$  interface in Figure 8 supported this mechanism, as grain-boundary  $\beta$  limited the extent of dislocation recovery by maintaining the interfacial misfit. The lack of ductility in this sample indicated that the dislocation structures were no longer acting as soft barriers for dislocations and additional mechanisms were operating which could hinder slip. The fact that V-rich dislocations were observed (Figure 9) indicated that solute redistribution was playing an important role in controlling dislocation slip, however, it could also be stated that O had a role to play in sample embrittlement.<sup>[52]</sup> There are also additional factors that may be affecting the mechanical performance of the material from the build process, such as porosity, residual stress, surface roughness and microstructural morphology.<sup>[53,54]</sup> However, it is anticipated this would reduce in statistical relevance due to the numerous tensile tests completed. Additional discussion of this can be found in Ali *et al.*<sup>[19]</sup>. Here, we discuss the observed evidence of differing defects and chemical segregation within the printed materials.

The presence of H and/or O due to process-related contamination has been known to strongly effect the elongation in specimens which could have happened to the ones built on a bed temperature of 770 °C, as these elements are well known to promote substantial reductions in ductility in Ti alloys.<sup>[31]</sup> It is common for samples produced *via* LPBF to contain increased oxygen content, particularly within the  $\alpha'$  phase.<sup>[55]</sup> This can be explained with the higher than required partial pressure of oxygen in the LPBF machine which leads to oxygen uptake during printing.<sup>[56]</sup> For instance, Tan *et al.*<sup>[7]</sup> measured high H and O levels (between 0.1 and 1 at. pct) in Ti-6Al-4V produced by EBM. It was previously indicated that oxygen increases the critical stress for martensite formation, and increased oxygen stabilises the  $\alpha$  phase whilst decreasing the ductility.<sup>[55]</sup> As increased substrate temperatures inhibit martensite, this could indicate that heating the substrate results in higher oxygen contents of the alloy.<sup>[57]</sup> The presence of any number of elements may aid the atomic shuffle required for the martensitic transformation, and therefore local composition is highly important.

To understand the effect of preheating temperatures on local changes in thermal history and microstructure, it is worth comparing the results from this work with results obtained by processing Ti-6Al-4V using other AM technologies. At a bed temperature of 100 °C, the microstructure was comparable to as-built microstructures obtained by conventional LPBF methods in

as-built conditions, which have reported very high cooling rate ( $\sim 10^6$  K/s) and lowest build temperature.<sup>[58]</sup> Yang *et al.* observed a high density of dislocation tangles, twins and fine-scale  $\beta$ ; they argued that fine-scale  $\beta$  is unstable due to their XRD results did not show  $\beta$  peaks.<sup>[59]</sup> The authors did, however, observe a shift in (110) peaks compared to calculated lattice parameters, which they attributed to the increased solubility of V in  $\alpha'$ , which was not confirmed experimentally. Other authors have argued that the peak shift is caused by solute redistribution.<sup>[15]</sup> Similar microstructures were reported by several authors,<sup>[58]</sup> however, no reports of elemental segregation at twins could be found.

On the other hand, the observed microstructure at a bed temperature of 570 °C was partially similar to microstructures obtained by LPBF after heat treating the samples at medium to low temperatures. For instance, Xu *et al.*<sup>[60]</sup> used SEM to characterise the microstructure of SLM Ti-6Al-4V in as-built state and after applying different heat treatments. The BackScatter Electron images (BSE) of the as-built samples did not show evidence of forming nano-scale  $\beta$  particles at grain boundaries, however, when post-LPBF tempering at 540 °C, isolated nano particles of  $\beta$  along the  $\alpha$  boundaries were observed. The authors also reported that the decomposition of martensite took place at temperatures as low as 400 °C. No elemental segregation at dislocations was reported.

The observed microstructure at a bed temperature of 770 °C was similar to microstructures obtained by Electron Beam Melting (EBM), where the cooling rate was less severe ( $\sim 10^4$  K/s) and the local build temperature was comparable.<sup>[61]</sup> For instance, Tan *et al.*<sup>[7]</sup> studied the transition of  $\beta$  to  $\alpha'$  and  $\alpha$  during EBM by means of atom probe and SEM. To do this they varied the thickness of the built samples to determine the variations in microstructure. Thin samples where fully martensitic and thick samples contained primarily  $\alpha + \beta$ . Their atom probe results showed local elemental enrichment (V) at dislocations in martensitic samples (thin) but no segregation at twins was reported, whereas the composition in the thick samples corresponded to that at equilibrium in an  $\alpha + \beta$  microstructure. They argued that discrete  $\beta$  particles form initially along the  $\alpha'$  plate boundaries and grow subsequently, however, they only referred to the low possibility of finding connecting  $\beta$  rods within the  $\alpha'$  plates.

The microstructures of Ti alloys were incredibly sensitive to thermal processing and thermal history. Parameters such as cooling rate, both above and below

the  $\beta$  transus, were critical to the resultant microstructure, which was directly linked to the final strength and fatigue performance.<sup>[52,62]</sup> Extended time at temperature due to substrate heating as seen here therefore acted as pseudo-ageing, comparable to standard processes. This had a significant effect on the local chemistry and diffusion and how this interacted with defects within the material, as well as microstructural evolution.

### B. Phase Transformation Kinetics and Their Relation with Martensite Transformation Parameters

The phase transformation sequence in Ti-6Al-4V produced by LPBF and EBM differed during the final stages but was similar during the initial stages of the thermal cycle,<sup>[7,59]</sup> which served as baseline for analysing the transformation sequence in the present work. The sequence for LPBF and EBM was as follows: during the first cycle,  $\beta$  forms upon solidification which rapidly transformed into  $\alpha'$  due to the very high cooling rates. During subsequent cycles,  $\alpha'$  partially transformed back to  $\beta$  upon reheating, which then transformed again to  $\alpha'$  upon cooling, leading to primary and secondary  $\alpha'$ . A small fraction of retained  $\beta$  remained during the build process and  $\alpha'$  eventually transformed to  $\alpha + \beta$  in EBM. In order to understand the differences in the primary phases observed at different preheating temperatures (Table II), it was important to also identify the transformation kinetics of  $\beta \rightarrow \alpha$  and  $\beta \rightarrow \alpha'$  in Ti-6Al-4V. The martensite start,  $M_s$ , and finish,  $M_f$ , temperatures were estimated as  $\sim 790^\circ\text{C}$  and  $\sim 710^\circ\text{C}$ , respectively,<sup>[63]</sup> however, the diffusional transformation from  $\beta$  to  $\alpha$  was highly dependent on the cooling rate and the local composition, which in itself had a significant effect on the undercooling. There is also evidence in the literature that a large variety of  $M_s$  temperatures are reported, from as high as  $800^\circ\text{C}$  to as low as  $575^\circ\text{C}$ , though there are a range of different factors that may affect this such as chemistry and starting microstructure.<sup>[64]</sup>

At a bed temperature of  $770^\circ\text{C}$ , the substrate was just below the  $M_s$  and above  $M_f$ , therefore less  $\alpha'$  formed during the first and subsequent thermal cycles and the substrate spent significantly longer in the  $\alpha + \beta$  phase field, leading to more energy being supplied for diffusion. As  $\alpha$  was a more stable preferable phase compared to  $\alpha'$ , and more prevalent at slower cooling rates, a lack of  $\alpha'$  was observed in this specimen. Possible slower cooling additionally meant that as the material was cooled through the  $\beta$  transus, significant phase change occurs. This was evident in the tangled dislocations in Figure 8 and the small  $\beta$  particles that were observed. Geometrically necessary dislocations were prevalent in these types of microstructures due to the misfit between the  $\alpha$  and  $\beta$  phases,<sup>[15,48,65]</sup> where the  $\beta$  phase was much larger, resulting in both a strain and rotation to create a favourable low energy interface.<sup>[66]</sup> Once the  $\beta$  phase had transformed upon cooling, these dislocations remained, and furthermore could explain the partitioning of  $\beta$  stabilisers to dislocations.

At a bed temperature of  $570^\circ\text{C}$ , higher undercooling promoted significant  $\alpha'$  formation, and  $\alpha$  nucleation was

thermodynamically favourable; as the preheating temperature was below  $M_f$ ,  $\alpha$  is likely to have nucleated from the  $\alpha'$  by solute partitioning. However, at this temperature the energy for chemical diffusion was lower, providing a much slower growth velocity for the  $\alpha$  phase.<sup>[23,67]</sup> Nano  $\beta$  was observed at this substrate temperature and was less prevalent than at  $770^\circ\text{C}$ , however, APT showed an increase of V at the  $\alpha/\alpha'$  boundary indicating a much finer presence of  $\beta$  within the microstructure.

This analysis also indicated that for substrate bed temperatures below  $570^\circ\text{C}$ , e.g., at  $100^\circ\text{C}$ , the microstructure was primarily martensitic with  $\alpha$  eventually forming, and a small fraction of  $\beta$  formation was possible, only if thermal energy was available for elemental diffusion.  $\alpha'$  decomposed above  $100^\circ\text{C}$ , as  $\alpha$  nucleation became more prolific, therefore leading primarily to  $\alpha + \beta$ .

As for other microstructural features, microtwinning in  $\alpha'$  was only observed when preheating at  $100^\circ\text{C}$ , whereas the IPF maps for  $570^\circ\text{C}$  and  $770^\circ\text{C}$  in Figure 2 a lamellar  $\alpha + \beta$  microstructure. However, the rapid phase change has clearly introduced residual strain into the specimens, and we could qualitatively compare the behaviour of twinning observed in the present work with that for mechanical twinning in Ti-6Al-4V deformed at different temperatures. Mechanical twinning in Ti-6Al-4V typically occurs only when samples are deformed at very high strain rates or very low temperatures.<sup>[68]</sup> Under such conditions, mechanical twinning formed up to a maximum deformation temperature of  $\sim 400^\circ\text{C}$  to  $450^\circ\text{C}$ . Hao *et al.*<sup>[69]</sup> reported in the near- $\alpha$  alloy Ti-6Al-2Zr-1Mo-V wt pct that twinning formed under tension at and below  $400^\circ\text{C}$ . Similarly, Zeng *et al.*<sup>[70]</sup> reported in commercially pure Ti that twinning was suppressed at  $650^\circ\text{C}$  and Fitzner *et al.*<sup>[71]</sup> reported that twinning formed at room temperature in near- $\alpha$  Ti-Al alloys with Al up to 12 at. pct, whereas for higher Al contents it was suppressed due to the activation of basal slip. Therefore, since twinning impeded dislocation motion and potentially lowered ductility, if the preheating occurred above  $400^\circ\text{C}$  to  $450^\circ\text{C}$ , the ductility could in principle be increased *via* promoting twin recovery.

### C. Elemental Partitioning Affects

Previous authors observed the presence of nano-scale  $\beta$  phase that increased with annealing at  $530^\circ\text{C}$  for 2 hours after building.<sup>[59]</sup> It is important to note that the observed increase in V concentration was up to 18 at. pct, which was much larger than the observed results in this manuscript ( $\sim 5$  at. pct). Most authors reported lath like  $\beta$  structures within both SLM and EBM structures.<sup>[7,12]</sup> However, the results from modelling of the effect of local defects and V content on the Gibbs-Free energy showed that it would take a much higher dislocation density to promote the heterogeneous nucleation of the  $\beta$  phase at these V rich regions (although there may be some errors in the measurement of dislocation density from a projected planar surface). The conclusion of our work was that the effect of a

heated substrate bed on the presence of the  $\beta$  phase was more likely to be a coarsening of an already present phase. However, it was also possible that these enriched regions were in fact a precursor to  $\beta$  platelet precipitation, which could be encouraged to grow into more pronounced  $\beta$  films after subsequent aging.<sup>[59]</sup>

The presence of local solute enrichment had a likely effect of the local strain field. It is known that the changing concentration of V in both the alpha and beta phases during heating has an effect of the lattice parameters, causing a difference in the expansion behaviours of both phases.<sup>[66]</sup> The presence of Al at microtwin boundaries had a similar effect and could in fact indicate an increase in the local stacking fault energy.<sup>[71]</sup> Therefore, changing solute concentrations could be affecting the strain in the lattice as microstructure formation occurs, causing an increased strain rate, leading to solute concentration at defects.

## VI. CONCLUSIONS

Samples of Ti-6Al-4V were produced through LPBF on a heated substrate between 100 °C and 770 °C. Increasing the temperature of the substrate from 100 °C to 570 °C improved the ductility during room temperature tensile tests, with 570 °C being the ductility maximum. Further heating of the substrate during sample production up to 770 °C reduced ductility to zero. Although the ductility changed significantly with processing conditions, the UTS at 100 °C and 570 °C was approximately constant (~ 1.2 GPa) and lowest at 770 °C due the alloy's brittle behaviour. Our analysis employed SEM, TEM and APT to study the complex variations in microstructure and solute behaviour to establish the specific mechanisms controlling the strength and ductility at different substrate temperatures. In summary:

- At a substrate temperature of 100 °C, a heavily strained and twinned microstructure, primarily composed of  $\alpha + \alpha'$ , was observed and it was comparable to as-built microstructures obtained by conventional LPBF methods. The low ductility of this sample was attributed to the high density of microtwins and dislocations preventing any further plasticity and/or dislocation slip.
- At a substrate temperature of 570 °C, twins were no longer present and instead nano-scale  $\beta$  precipitates were observed within  $\alpha'$  and  $\alpha$ , as well as dislocation networks. The lack of twins was attributed to this temperature being higher than the temperature for twin recovery in Ti-6Al-4V (~ 400 °C to 450°C). The microstructure was partially similar to microstructures obtained by conventional LPBF after heat treating the samples at medium to low temperatures.
- At a substrate temperature of 770 °C, the phase fraction of  $\beta$  increased, at the expense of  $\alpha'$ , and dislocation tangles formed within the  $\alpha$  grain interiors. The microstructure was similar to microstructures obtained by Electron Beam Melting, where the

local build temperature was comparable and the cooling rates were less severe, leading to a mix of  $\alpha + \beta$  and small residual  $\alpha'$ . Though the microstructures are comparable, there is a drastic reduction in the tensile strength, presenting as much more brittle than expected.

- Dislocation networks observed at a 570 °C bed temperature have likely formed by a sequence of interfacial dislocations generating at the  $\alpha'/\beta$  interface, as  $\alpha'$  nucleates during rapid cooling. We concluded that dislocation networks in the acted as "soft barriers" for slip and helped increase ductility.
- The dislocation tangles observed at a 770 °C bed temperature formed by a similar mechanism, but the higher build temperature promoted extensive recovery and partial network dissolution. The lack of ductility was attributed to local solute redistribution causing dislocation pinning and an increase of O content in this sample, particularly at  $\alpha'$  where a high dislocation density is present.
- Solute segregation at crystal defects was observed in all pre-heating conditions. Al and V segregation at microtwins was observed at a substrate temperature of 100 °C, with mutually exclusive Al- and V-rich regions forming in adjacent twins. This indicated that the shear strain induced by twinning induced a sufficient driving force to cause solute partitioning and short range diffusion towards forming  $\alpha$  and  $\beta$  in the Al- and V-rich regions. To the authors knowledge, it is the first time such "selective" solute partitioning at twins is observed in Ti.
- V segregation at dislocations was observed at a substrate temperature of 570 °C and 770 °C, consistent with the higher preheating temperatures. The observations were in agreement with previous reports in Ti-6Al-4V produced by Electron Beam Powder Fusion, and with dislocation diffusion models.
- High O contents were measured in all samples. O contents at a substrate temperature of 770 °C were just above the threshold for O embrittlement, therefore the sample showed a lack of ductility. At a substrate temperature of 100 °C and 570 °C, the O was measured below the critical threshold, as shown in Table I.
- Based on the complicated phase transformation sequences and microstructural variations analysed this work, optimal *in-situ* heat treatments for improved microstructural control and mechanical properties were expected in the temperature range of 450 °C to 570 °C. This processing window resulted in a strong (~ 1.2 GPa) and fine  $\alpha' + \alpha + \beta$  structure containing a high density of dislocation networks, acting as soft barriers for slip increasing the ductility. The relatively-high temperatures also promoted short-range diffusion for solute segregation and localised solid solution strengthening for improved strength. This temperature range produced samples below the critical Oxygen content for severe embrittlement, whilst the O adsorbed during the build process may promote additional solid solution strengthening, although the actual

levels of O absorption are material, machine and process-specific.

## ACKNOWLEDGMENTS

E.I. Galindo-Nava and T. B. Britton would all like to acknowledge the Royal Academy of Engineering for their research fellowships and S. Pedrazzini for her associate research fellowship. E.I. Galindo-Nava performed this work under EPSRC grant EP/T008687/1. S. Pedrazzini performed part of this work under EPSRC grant EP/M005607/1 and under EPSRC fellowship EP/S0138881/1. Giorgio Divitini is gratefully acknowledged for his help with TEM. P. Bajaj acknowledges funding by the DFG under grant number JA2482/2-1. EPSRC Future Manufacturing Hub in Manufacture using Advanced Powder Processes (MAPP)(EP/P006566/1) is acknowledged for their support during this investigation. T. Dessolier and T. B. Britton acknowledge funding from the Shell-Imperial Advances Interfacial Materials Science (AIMS) Centre.

## CONFLICT OF INTEREST

On behalf of all authors, the corresponding author states that there is no conflict of interest.

## OPEN ACCESS

This article is licensed under a Creative Commons Attribution 4.0 International License, which permits use, sharing, adaptation, distribution and reproduction in any medium or format, as long as you give appropriate credit to the original author(s) and the source, provide a link to the Creative Commons licence, and indicate if changes were made. The images or other third party material in this article are included in the article's Creative Commons licence, unless indicated otherwise in a credit line to the material. If material is not included in the article's Creative Commons licence and your intended use is not permitted by statutory regulation or exceeds the permitted use, you will need to obtain permission directly from the copyright holder. To view a copy of this licence, visit <http://creativecommons.org/licenses/by/4.0/>.

## REFERENCES

1. R.R. Boyer: *Adv. Perform. Mater.*, 1995, vol. 2, pp. 349–68.
2. R.R. Boyer: *Mater. Sci. Eng. A*, 1996, vol. 213, pp. 103–14.
3. S. Liu and Y.C. Shin: *Mater. Des.*, 2019, vol. 164, p. 107552.
4. L.P. Borrego, J.A.M. Ferreira, J.D.M. Costa, C. Capela, and J. De Jesus: *Procedia Struct. Integrity*, 2018, vol. 13, pp. 1000–05.
5. C. Zhang, J. Zhu, H. Zheng, H. Li, S. Liu, and G.J. Cheng: *Int. J. Extreme Manuf.*, 2020, vol. 2, p. 032003.
6. K.S. Chan, M. Koike, R.L. Mason, and T. Okabe: *Metall. Mater. Trans. A.*, 2013, vol. 44A, pp. 1010–22.
7. X. Tan, Y. Kok, W.Q. Toh, Y.J. Tan, M. Descoins, D. Mangelinck, S.B. Tor, K.F. Leong, and C.K. Chua: *Sci. Rep.*, 2016, vol. 6, pp. 1–10.

8. S. Cao, R. Chu, X. Zhou, K. Yang, Q. Jia, C.V.S. Lim, A. Huang, and X. Wu: *J. Alloy Compd.*, 2018, vol. 744, pp. 357–63.
9. J. Yang, H. Yu, J. Yin, M. Gao, Z. Wang, and X. Zeng: *Mater. Des.*, 2016, vol. 108, pp. 308–18.
10. T. Vilaro, C. Colin, and J.D. Bartout: *Metall. Mater. Trans. A*, 2011, vol. 42A, pp. 3190–99.
11. W. Xu, E.W. Lui, A. Pateras, M. Qian, and M. Brandt: *Acta Mater.*, 2017, vol. 125, pp. 390–400.
12. X.-Y. Zhang, G. Fang, S. Leeßang, A.J. Böttger, A.A. Zadpoor, and J. Zhou: *J. Alloy Compd.*, 2018, vol. 735, pp. 1562–75.
13. B. Vrancken, L. Thijs, J. Kruth, and J. Van Humbeeck: *J. Alloy Compd.*, 2012, vol. 541, pp. 177–85.
14. Y. Sakurai and K. Kakehi: *J. Jpn. Inst. Metals Mater.*, 2017, pp. 120–26.
15. G. Li, J. Li, X. Tian, X. Cheng, B. He, and H. Wang: *Mater. Sci. Eng. A*, 2017, vol. 684, pp. 233–38.
16. S. Leuders, S. Meiners, L. Wu, A. Taube, T. Tröster, and T. Niendorf: *J. Mater. Process. Technol.*, 2017, vol. 248, pp. 130–42.
17. S. Tammas-williams, P.J. Withers, I. Todd, and P.B. Prangnell: *Metall. Mater. Trans. A*, 2016, vol. 47A, pp. 1939–46.
18. M. Benedetti, M. Cazzolli, V. Fontanari, and M. Leoni: *Procedia Struct. Integrity*, 2016, vol. 2, pp. 3158–67.
19. H. Ali, L. Ma, H. Ghadbeigi, and K. Mumtaz: *Mater. Sci. Eng. A*, 2017, vol. 695, pp. 211–20.
20. D. Raabe, M. Herbig, S. Sandlöbes, Y. Li, D. Tytko, M. Kuzmina, D. Ponge, and P. Choi: *Curr. Opin. Solid State Mater. Sci.*, 2014, vol. 18, pp. 253–61.
21. L.R. Zeng, H.L. Chen, X. Li, L.M. Lei, and G.P. Zhang: *J. Mater. Sci. Technol.*, 2018, vol. 34, pp. 782–87.
22. M.J. Bermingham, D.H. StJohn, J. Krynen, S. Tedman-Jones, and M.S. Dargusch: *Acta Mater.*, 2019, vol. 168, pp. 261–74.
23. A.K. Ackerman, A.J. Knowles, H.M. Gardner, A.A.N. Németh, I. Bantounas, A. Radecka, M.P. Moody, P.A.J. Bagot, R.C. Reed, D. Rugg, and D. Dye: *Metall. Mater. Trans. A*, 2020, vol. 51A, pp. 131–41.
24. A.K. Ackerman, V.A. Vorontsov, I. Bantounas, Y. Zheng, Y. Chang, T. McAuliffe, W.A. Clark, H.L. Fraser, B. Gault, D. Rugg, and D. Dye: *Phys. Rev. Mater.*, 2020, vol. 4, pp. 1–7.
25. H. Zhao, F. De Geuser, A. Kwiatkowski da Silva, A. Szczepaniak, B. Gault, D. Ponge, and D. Raabe: *Acta Mater.*, 2018, vol. 156, pp. 318–29.
26. *E8/E8M-13a, Standard Test Methods for Tension Testing of Metallic Materials*, ASTM International, West Conshohocken, PA, 2013.
27. D. Blavette, A. Bostel, J.M. Sarrau, B. Deconihout, and A. Menand: *Nature*, 1993, vol. 363, pp. 432–35.
28. B. Gault, D. Haley, F. de Geuser, M.P. Moody, E.A. Marquis, D.J. Larson, and B.P. Geiser: *Ultramicroscopy*, 2011, vol. 111, pp. 448–57.
29. P. Chen, F. Wang, J. Ombogo, and B. Li: *Mater. Sci. Eng. A*, 2019, vol. 739, pp. 173–85.
30. X. Tan, Y. Kok, Y. Jun, G. Vastola, Q. Xiang, G. Zhang, Y. Zhang, S. Tor, K. Fai, and C. Kai: *J. Alloy Compd.*, 2015, vol. 646, pp. 303–09.
31. H. Conrad: *Prog. Mater. Sci.*, 1981, vol. 26, pp. 123–403.
32. P. Kontis, Z. Li, M. Segersäll, J.J. Moverare, R.C. Reed, D. Raabe, and B. Gault: *Metall. Mater. Trans. A*, 2018, vol. 49A, pp. 4236–45.
33. A.J. London, S. Lozano-Perez, M.P. Moody, S. Amirthapandian, B.K. Panigrahi, C.S. Sundar, and C.R.M. Grovenor: *Ultramicroscopy*, 2015, vol. 159, pp. 360–67.
34. A.S. Gornakova and S.I. Prokofjev: *J. Mater. Sci.*, 2020, vol. 55, pp. 9225–36.
35. M. Villa, J.W. Brooks, R.P. Turner, H. Wang, F. Boitout, and R.M. Ward: *Metall. Mater. Trans. B*, 2019, vol. 50B, pp. 2898–2911.
36. A.T. Dinsdale: *Calphad*, 1991, vol. 15, pp. 317–425.
37. G. Suprobo, A.A. Ammar, N. Park, E.R. Baek, and S. Kim: *Met. Mater. Int.*, 2019, vol. 25, pp. 1428–35.
38. E. Bouchaud, L. Kubin, and H. Octor: *Metall. Trans. A*, 1991, vol. 22, pp. 1021–28.
39. Y. Yang, Y.J. Liu, J. Chen, H.L. Wang, Z.Q. Zhang, Y.J. Lu, S.Q. Wu, and J.X. Lin: *Mater. Sci. Eng. A*, 2017, vol. 707, pp. 548–58.
40. K. Kim, J. Lee, H. Kim, and Z. Lee: *Appl. Microsc.*, 2014, vol. 44, pp. 74–78.



41. R.P. Elliot: *Diffusion in Titanium and Titanium Alloys*, Chicago, Illinois, 1962.
42. G. Lindwall, K.W. Moon, Z. Chen, M. Mengason, M.E. Williams, J.M. Gorham, J.C. Zhao, and C.E. Campbell: *J. Phase Equilib. Diffus.*, 2018, vol. 39, pp. 731–46.
43. D. Caillard and J.L.B.T.-P.M.S. Martin, eds.: in *Thermally Activated Mechanisms in Crystal Plasticity*, Pergamon, 2003, vol. 8, pp. 57–82.
44. L.E. Murr, S.A. Quinones, S.M. Gaytan, M.I. Lopez, A. Rodela, E.Y. Martinez, D.H. Hernandez, E. Martinez, F. Medina, and R.B. Wicker: *J. Mech. Behav. Biomed. Mater.*, 2009, vol. 2, pp. 20–32.
45. D. Barba, E. Alabort, S. Pedrazzini, D.M. Collins, A.J. Wilkinson, P.A.J. Bagot, M.P. Moody, C. Atkinson, A. Jérusalem, and R.C. Reed: *Acta Mater.*, 2017, vol. 135, pp. 314–29.
46. J. He, C.H. Zenk, X. Zhou, S. Neumeier, D. Raabe, B. Gault, and S.K. Makineni: *Acta Mater.*, 2020, vol. 184, pp. 86–99.
47. E.I. Galindo-Nava: *Scripta Mater.*, 2017, vol. 138, pp. 6–11.
48. S. Joseph, I. Bantounas, T.C. Lindley, and D. Dye: *Int. J. Plast.*, 2018, vol. 100, pp. 90–103.
49. R.K. Rai, J.K. Sahu, S.K. Das, N. Paulose, D.C. Fernando, and C. Srivastava: *Mater. Charact.*, 2018, vol. 141, pp. 120–28.
50. C.J. Szczepanski, S.K. Jha, J.M. Larsen, and J.W. Jones: *Metall. Mater. Trans. A*, 2012, vol. 43A, pp. 4097–4112.
51. F. Bridier, P. Villechaise, and J. Mendez: *Acta Mater.*, 2008, vol. 56, pp. 3951–62.
52. D.P. Satko, J.B. Shaffer, J.S. Tiley, S.L. Semiatin, A.L. Pilchak, S.R. Kalidindi, Y. Kosaka, M.G. Glavivic, and A.A. Salem: *Acta Mater.*, 2016, vol. 107, pp. 377–89.
53. J.M. Oh, B.G. Lee, S.W. Cho, S.W. Lee, G.S. Choi, and J.W. Lim: *Met. Mater. Int.*, 2011, vol. 17, pp. 733–36.
54. Y. Chong, R. Zhang, M.S. Hooshmand, S. Zhao, D.C. Chrzan, M. Asta, J.W. Morris, and A.M. Minor: *Nat. Commun.*, 2021, vol. 12(1), p. 6158.
55. M. Yan, W. Xu, M.S. Dargusch, H.P. Tang, M. Brandt, and M. Qian: *Powder Metall.*, 2014, vol. 57, pp. 251–57.
56. W.-H. Lee, T.-W. Na, K.-W. Yi, S.-M. Yang, J.-W. Kang, H.G. Kim, and H.-K. Park: *Rapid Prototyping J.*, 2020, vol. 26(8), pp. 1401–04.
57. D. Banerjee and J.C. Williams: *Acta Mater.*, 2013, vol. 61, pp. 844–79.
58. S. Gorsse, C. Hutchinson, M. Gouné, and R. Banerjee: *Sci. Technol. Adv. Mater.*, 2017, vol. 18, pp. 584–610.
59. J. Haubrich, J. Gussone, P. Barriobero-vila, P. Kürsteiner, D. Raabe, N. Schell, G. Requena, and A.J. Eric: *Acta Mater.*, 2019, vol. 167, pp. 136–48.
60. W. Xu, M. Brandt, S. Sun, J. Elambasseril, Q. Liu, K. Latham, K. Xia, and M. Qian: *Acta Mater.*, 2015, vol. 85, pp. 74–84.
61. C. Körner: *Int. Mater. Rev.*, 2016, vol. 61, pp. 361–77.
62. G. Lütjering: *Mater. Sci. Eng. A*, 1998, vol. 243, pp. 32–45.
63. R. Dabrowski: *Arch. Metall. Mater.*, 2011, vol. 56, pp. 703–07.
64. S.S. Al-Bermani, M.L. Blackmore, W. Zhang, and I. Todd: *Metall. Mater. Trans. A*, 2010, vol. 41A, pp. 3422–34.
65. R.C. Pond, S. Celotto, and J.P. Hirth: *Acta Mater.*, 2003, vol. 51, pp. 5385–98.
66. J.W. Elmer, T.A. Palmer, S.S. Babu, and E.D. Specht: *Mater. Sci. Eng. A*, 2005, vol. 391, pp. 104–13.
67. S. Mironov, M. Murzinova, S. Zherebtsov, G.A. Salishchev, and S.L. Semiatin: *Acta Mater.*, 2009, vol. 57, pp. 2470–81.
68. D.G.L. Prakash, R. Ding, R.J. Moat, I. Jones, P.J. Withers, J.Q. da Fonseca, and M. Preuss: *Mater. Sci. Eng. A*, 2010, vol. 527, pp. 5734–44.
69. F. Hao, J. Xiao, Y. Feng, Y. Wang, J. Ju, Y. Du, K. Wang, L. Xue, Z. Nie, and C. Tan: *J. Market. Res.*, 2020, vol. 9, pp. 2818–31.
70. Z. Zeng, Y. Zhang, and S. Jonsson: *Mater. Sci. Eng. A*, 2009, vol. 513–514, pp. 83–90.
71. A. Fitzner, D.G.L. Prakash, J.Q. da Fonseca, M. Thomas, S.-Y. Zhang, J. Kelleher, P. Manuel, and M. Preuss: *Acta Mater.*, 2016, vol. 103, pp. 341–51.

**Publisher's Note** Springer Nature remains neutral with regard to jurisdictional claims in published maps and institutional affiliations.